





Numerical study of heat transfer in Rayleigh-Bénard convection under rarefied gas conditions

B. Goshayeshi ¹, G. Di Staso ¹, F. Toschi ^{1,2,3} and H. J. H. Clercx ^{1,*}

¹*Fluid Dynamics Laboratory and J.M. Burgers Center for Fluid Dynamics, Department of Applied Physics, Eindhoven University of Technology, P. O. Box 513, 5600 MB Eindhoven, The Netherlands*

²*Centre of Analysis, Scientific Computing, and Applications W&I, Department of Mathematics and Computer Science, Eindhoven University of Technology, P. O. Box 513, 5600 MB Eindhoven, The Netherlands*

³*Istituto per le Applicazioni del Calcolo, Consiglio Nazionale delle Ricerche, 00185 Rome, Italy*



(Received 1 December 2019; accepted 24 June 2020; published 7 July 2020)

The focus of this research is to delineate the thermal behavior of a rarefied monatomic gas confined between horizontal hot and cold walls, physically known as rarefied Rayleigh-Bénard (RB) convection. Convection in a rarefied gas appears only for high temperature differences between the horizontal boundaries, where nonlinear distributions of temperature and density make it different from the classical RB problem. Numerical simulations adopting the direct simulation Monte Carlo approach are performed to study the rarefied RB problem for a cold to hot wall temperature ratio equal to $r = 0.1$ and different rarefaction conditions. Rarefaction is quantified by the Knudsen number, Kn . To investigate the long-time thermal behavior of the system two ways are followed to measure the heat transfer: (i) measurements of macroscopic hydrodynamic variables in the bulk of the flow and (ii) measurements at the microscopic scale based on the molecular evaluation of the energy exchange between the isothermal wall and the fluid. The measurements based on the bulk and molecular scales agreed well. Hence, both approaches are considered in evaluations of the heat transfer in terms of the Nusselt number, Nu . To characterize the flow properly, a modified Rayleigh number (Ra_m) is defined to take into account the nonlinear temperature and density distributions at the pure conduction state. Then the limits of instability, indicating the transition of the conduction state into a convection state, at the low and large Froude asymptotes are determined based on Ra_m . At the large Froude asymptote, simulations following the onset of convection showed a relatively small range for the critical Rayleigh ($\text{Ra}_m = 1770 \pm 15$) that flow instability occurs at each investigated rarefaction degree. Moreover, we measured the maximum Nusselt values Nu_{max} at each investigated Kn . It was observed that for $\text{Kn} \geq 0.02$, Nu_{max} decreases linearly until the transition to conduction at $\text{Kn} \approx 0.03$, known as the rarefaction limit for $r = 0.1$, occurs. At the low Froude (parametric) asymptote, the emergence of a highly stratified flow is the prime suspect of the transition to conduction. The critical Ra_m in which this transition occurs is then determined at each Kn . The comparison of this critical Rayleigh versus Kn also shows a linear decrease from $\text{Ra}_m \approx 7400$ at $\text{Kn} = 0.02$ to $\text{Ra}_m \approx 1770$ at $\text{Kn} \approx 0.03$.

DOI: [10.1103/PhysRevE.102.013102](https://doi.org/10.1103/PhysRevE.102.013102)

I. INTRODUCTION

Thermal convection, the flow of a fluid due to temperature gradients, is a frequent process in nature and technology. The dynamics of such process can be found in many natural phenomena such as circulations in the oceans [1–3], atmospheric flows [2,4,5], the dynamics of the interior core of stars and planets [6–8], geostrophic convection [1,9–14], as well as in numerous industrial applications like heat exchangers and passive cooling devices for electronic equipments and computer chips [15]. Moreover, there are high-tech applications where precise knowledge of thermal convection phenomena is very important. Thermal control of electronics using the micro- and nanoelectromechanical systems (MEMS/NEMS) [16] and the thermal management of the extreme ultraviolet (EUV) radiation source facilities in vacuum environments [17,18], which are used in manufacturing of semiconductor devices, are only a few examples of these high-tech appli-

cations. Although the physics of these processes is generally complex, a simple thermal model is needed in order to represent the basic dynamics of all the cases mentioned above.

A fluid restricted between two parallel horizontal flat plates exposed to heating from below, cooling from the top and in presence of a vertical gravitational force is known as the Rayleigh-Bénard (RB) problem. This is a well-known physical system that is extensively studied in the framework of hydrodynamic stability theory [19,20]. In Rayleigh-Bénard convection, buoyancy due to density differences stimulated by temperature variations appear as the driving force of convection and is being counteracted by diffusion as an equilibrating fluid property. Thus, the RB system can be considered as a simple paradigm for the flow cases with the presence of thermal convection. It is also a reliable study setting for investigation of heat transfer, flow structure formation, fluid dynamic instability, and chaotic behavior in fluids [21], as well as of turbulence transition and thermally driven turbulence [22–25].

In continuum fluid dynamics, the intermolecular separation distances, known as the gas mean free path λ , are much

*h.j.h.clercx@tue.nl

smaller than the characteristic length scale of the flow. Under the continuum hypothesis and small temperature differences, the physics of RB convection can be described within the Oberbeck-Boussinesq (OB) framework [26–28], where the buoyancy force is a linear function of the temperature difference. In this case, the following two dimensionless numbers are sufficient to fully characterize the system: the Rayleigh number $Ra = \frac{\alpha g \Delta T H^3}{\nu k}$ and the Prandtl number $Pr = \frac{\nu}{k}$, where α is the thermal expansion coefficient, ν is the kinematic viscosity, k is the thermal diffusion coefficient, H is the distance between the horizontal hot and cold flat plates, and ΔT is the temperature difference between the plates.

Hitherto it is assumed that the fluid flow can be described with a continuum approach. However, for rarefied gases, the ratio of the molecular mean free path λ and the characteristic length scale, H in case of RB convection, is no longer negligible, and the continuum hypothesis becomes invalid. The Knudsen number $Kn = \lambda/H$ is a parameter used to determine the degree of rarefaction and is commonly used to classify flows based on rarefaction conditions. When the Knudsen number approaches zero, which basically occurs when $Kn \lesssim 0.001$, the flow regime is assumed continuum and to investigate the flow, Navier-Stokes equations (and eventually in the Boussinesq approximation) are accurate. Whereas, at large Knudsen numbers, for example when $Kn \gtrsim 10$, the free molecular regime dominates, where the most important physical phenomenon is the collision of particles with surfaces. Between these two limits, the slip-flow regime ($0.001 \lesssim Kn \lesssim 0.1$) and the transitional regime ($0.1 \lesssim Kn \lesssim 10$) can be found, and both the intermolecular and particle-to-surface collisions become physically important. In the slip-flow regime, which is the focus of the current investigation, the rarefaction effects are more important in the regions close to the walls, where phenomena such as slip velocity and temperature jump emerge [29].

Primarily rarefaction is recognized as one of the restricting factors for the occurrence of convection [30,31], and studying the RB convection outside the regime where the continuum fluid dynamics hypothesis can be applied requires other nondimensional control parameters than Ra and Pr . Furthermore, in order to be able to study the RB convection in the rarefied slip-flow regime, it is necessary to consider a case with high temperature differences, see Sec. II A. For instance, at a rarefied RB system using the isothermal wall conditions with the temperature ratio between the cold and hot walls, $r = T_c/T_h = 0.1$, convection is viable up to $Kn \lesssim 0.03$ [31], whereas for a case with low temperature variation, e.g., $r = 0.95$, convection is achievable only for continuum cases which practically means that $Kn \lesssim 0.001$. Thus, the temperature ratio r is another factor that influences the convection zone in rarefied RB flow. It is worth noticing that the range of Oberbeck-Boussinesq validity is an accurate assumption if $\alpha \Delta T \lesssim 0.2$ [25]. Therefore, for a large temperature difference of $r = 0.1$, the expansion coefficient set to $\alpha = 1/T_{\text{avg}}$, thus using the ideal gas assumption, and $T_{\text{avg}} = \frac{1}{2}(T_h + T_c)$, then $\alpha \Delta T = \frac{2(1-r)}{(1+r)} \approx 1.64$, and obviously non-Oberbeck-Boussinesq (NOB) effects emerge. It should be noted here that $\alpha \Delta T$ is not necessarily the determining factor for NOB effects. Further criteria have been proposed

[25,32,33] and discussions can be found in these studies. However, the criterion used in the present study as the typical threshold to assume NOB effects is $\alpha \Delta T \gtrsim 0.1$. In our investigation NOB effects are thus for sure present without even exploring the other indicators. Notice that considering a hard-sphere gas, Ra will be a function of (r, Kn, Fr) [34] with the Froude number defined as $Fr = \frac{V_{\text{th}}^2}{gH}$, where $V_{\text{th}} = \sqrt{2RT_h}$ is the most probable molecular speed at the hot wall, g is the acceleration due to gravity, and $R = \frac{k_B}{m}$ is the specific gas constant satisfying the ideal gas law according to $P = \rho RT$. Here k_B is the Boltzmann constant ($k_B \approx 1.38 \times 10^{-23}$ J/K) and m is the molecular mass. Hence, in general, a combination of three parameters from a set consisting of (r, Kn, Ra, Fr) is sufficient to appropriately delineate the convection state in a rarefied RB system.

In order to take care of rarefied effects and large temperature or density variations in numerical simulations, it is needed to apply a standard method based on the molecular description of the flow, where the Boltzmann equation is solved on the corresponding system [30,31]. The direct simulation Monte Carlo (DSMC), introduced by Bird [35–37], is a well-tested particle-based Monte Carlo simulation method to study nonequilibrium rarefied gas flows. The underlying principle of the DSMC method is to decouple the motion and collision (change of velocities) of particles at each time step into two sequential stages of free molecular movement and then binary collisions. During these stages the linear momentum and energy of colliding particles are conserved. Each particle or “simulator” represents a large group of gas molecules and the computational domain is divided into grid cells smaller than the gas mean free path. Collision pairs are then selected according to a stochastic binary collision scheme [38,39] within the cell or among available subcells in the cell [40]. Nanbu [41] and Wagner [42] proved that the DSMC method correctly solves the Boltzmann equation if the time step and the grid size become close to zero and the number of simulators tends toward the number of molecules within the flow field.

DSMC has already been used to investigate the RB convection in a rarefied gas on the formation of the convective rolls [31,34,43–46], on the chaotic and periodic behaviors of the flow [47], and on the transition of the flow into convection based on temperature [48] and heat-flux [49] evaluations. Stefanov *et al.* [31,44] used the DSMC method to recognize the onset of convection in rarefied RB flow of a hard-sphere gas based on three governing parameters (r, Kn, Fr) . In Ref. [31] an exact solution of the pure conduction state is provided and two analytical conditions for large and small Froude numbers, indicated as exterior bounds for the appearance of a convective state, are also determined. The critical Rayleigh number $Ra = 1708$, determined by linear stability analysis of the Oberbeck-Boussinesq equation [19], was assumed in the DSMC studies of the corresponding system [31] as an approximate exterior bound of convection at large Froude parameters.

The critical Rayleigh number $Ra = 1708$ is derived from a set of assumptions that does not entirely match with the physics governing the rarefied RB convection. For instance, as mentioned before, in the Boussinesq flow conditions

compressibility effects that originate from density variations and relative temperature differences are neglected [28]. Moreover, no-slip boundary conditions are assumed. Hence, this classical view does not conform with the RB convection in a rarefied gas with the presence of non-Oberbeck-Boussinesq effects caused by high temperature differences and presence of slip and temperature jump at the walls [31,50,51].

Manela and Frankel [50,52,53] applied the linear temporal stability analysis to the analytical solution of the rarefied RB problem to study the instability at low- and large-Fr limits, as well as with respect to the particle interaction model which was the variable hard-sphere model. Manela and Frankel [50] derived the neutral curves in the (Fr, Kn) plane that delineates the transition from the pure conduction to the convection state. They considered a modified Ra, defined by Golshtein and Elperin [34] for a hard-sphere gas, and showed that the derived neutral curves are asymptotically equivalent with a line of constant Rayleigh ($Ra \approx 1773$) at $r = 0.1$ and $Kn < 0.01$ in the (Fr, Kn) plane. Recently, Ben-Ami and Manela [54] replaced the isothermal wall conditions by the heat-flux boundary conditions and applied the linear temporal stability to the problem. They demonstrated that the heat-flux boundary causes destabilizing effects, extending the convection zone limits to a lower critical Rayleigh (at the onset of convection) and higher rarefaction limits.

Within this framework, the aim of the present research is to study the thermal behavior of rarefied RB convection with DSMC simulations over a large range of parameters. Although there are DSMC studies of three-dimensional RB convection [46,55], they are computationally expensive to be used in studies with a large span of parameters. In the present paper, therefore, we consider a two-dimensional Rayleigh-Bénard system of a “hard-sphere” gas at $r = 0.1$ and aspect ratio of 2, as studied in Refs. [31,50]. Focus is given on the higher rarefaction part with $Kn \in [0.015 - 0.03]$, where slip effects are more dominant. The parallelized DSMC code employed in this study is implemented and validated by Di Staso [56], see Sec. III. DSMC simulations are performed to determine the final thermal state of the system as convective or conductive, while the criterion is based on the Nusselt values obtained from heat transfer measurements in the bulk flow or at the molecular scale adjacent to the walls. Considering this criterion based on heat transfer evaluations, three distinct stages of thermal variations in the RB system are identified as (i) onset of convection, (ii) maximum convection, and (iii) cessation of convection and are addressed and quantified according to a modified Rayleigh number adapted with nonlinear temperature and density distributions at the pure conduction state.

In Sec. II, the 2D rarefied RB flow configuration will be described and two methods to evaluate heat transfer will be introduced. Subsequently, in Sec. III we briefly introduce the parallelized DSMC method employed in this work. The (Fr, Kn) parameter regime will be explored in Sec. IV. It starts with describing and illustrating the general flow behaviors, such as the rarefaction effect on convection. It then continues with investigations for understanding the onset of convection, determination of the maximum of convection, and the cessation of convection. Section V summarizes the conclusions of this research.

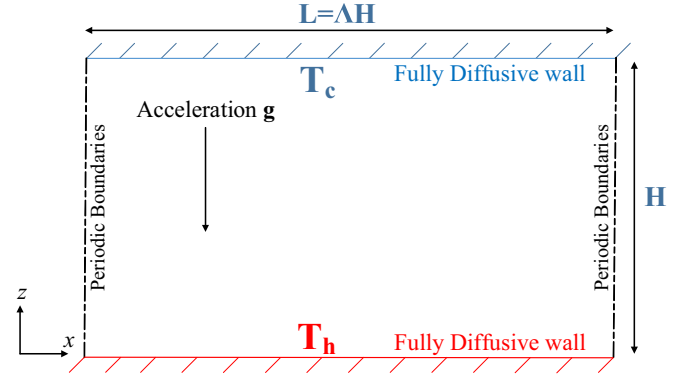


FIG. 1. Schematic of the 2D Rayleigh-Bénard flow configuration, where in the current study following considerations are selected: hard-sphere monatomic gas, aspect ratio of the domain $\Lambda = \frac{L}{H} = 2$, the temperature ratio $r = \frac{T_c}{T_h} = 0.1$, and fully accommodating diffusive surfaces.

II. RB FLOW ANALYSIS

A. Problem configuration

The schematic view of the two-dimensional RB cell employed in this study is given in Fig. 1. An initially quiescent monatomic hard-sphere model gas is confined between horizontal hot and cold isothermal walls at a temperature set of $(T_c, T_h) = (16, 160)$ K and a vertical separation distance equal to H . The confined gas is subject to a constant acceleration in the negative z direction, thus $\mathbf{g} = (0, -g)$. Gas molecules have purely diffuse reflections at the isothermal and fully accommodating surfaces.

In this system, the convection regime can be identified with three nondimensional numbers (r, Kn, Fr) . Here $Kn = \frac{\lambda}{H}$, where for a hard-sphere monatomic gas with diameter d and number density of n , we can define the mean free path λ according to $\lambda = \frac{1}{\sqrt{2}\pi d^2 n}$ [37]. An analytical solution of the mentioned Rayleigh-Bénard flow in a rarefied gas is only available for the pure conduction state and is derived in Ref. [31]. They considered the continuity, Navier-Stokes, energy and state equations for a perfect compressible viscous gas, with transport coefficients obtained from the Chapman-Enskog theory for low Knudsen numbers [57] for the hard-sphere gas model. The Prandtl number (Pr) and the ratio γ of specific heats at constant pressure are $Pr = 2/3$ and $\gamma = 5/3$, respectively. According to Stefanov *et al.* [31], the solution of these equations for the pure conduction state will lead to the following expressions for the temperature $T(z)$ and density $\rho(z)$ along the vertical direction z . For convenience, we assume dimensionless spatial coordinates with respect to the height H , i.e., $x \in [0 : 2]$ and $z \in [0 : 1]$, in these expressions,

$$T(z) = (\xi z + \zeta)^{2/3}, \quad (1)$$

$$\rho^*(z) = \frac{1}{T(z)} \exp \left[\frac{3\eta}{\xi} \sqrt{T(z)} \right], \quad (2)$$

$$\rho_t = \int_0^1 \rho^*(z) dz, \quad \rho(z) = \frac{\rho^*(z)}{\rho_t}, \quad (3)$$

$$\xi = T_1^{3/2} - T_0^{3/2} < 0, \quad \zeta = T_0^{3/2}, \quad \eta = -2/Pr,$$

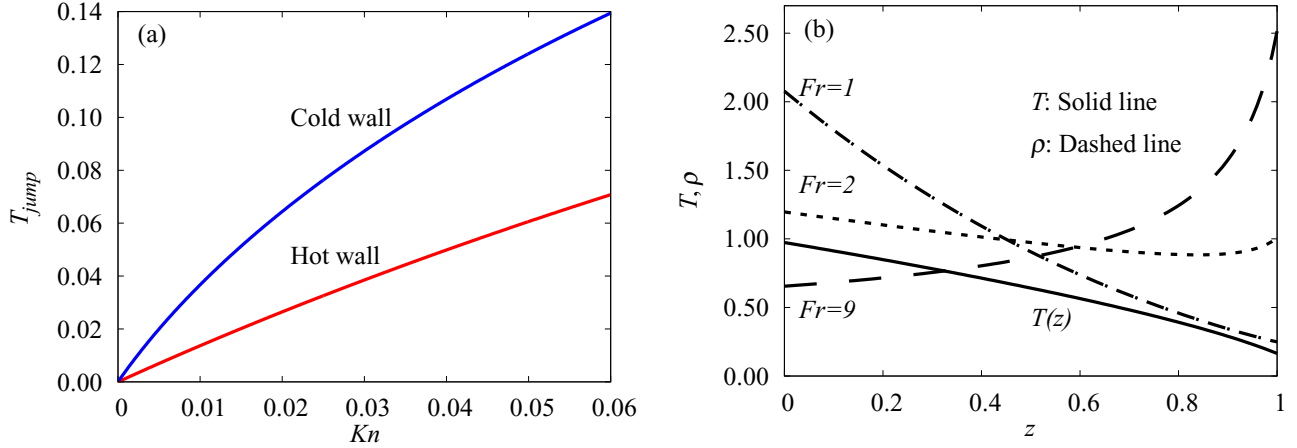


FIG. 2. The analytical solution in a rarefied RB cell for the pure conduction state: (a) Variation of the temperature jump T_{jump} based on the slip coefficients originated from the Bhatnagar-Gross-Krook (BGK) model [58] versus Kn at the hot and cold walls, (b) temperature (solid line) and density (dashed lines) profiles using Eqs. (1) and (2) obtained at parametric values of $r = 0.1$, $Kn = 0.02$, and $Fr = 1, 2$, and 9 .

where T_0 and T_1 , representing the temperature of the fluid adjacent to the walls, are obtained from the temperature jump boundary conditions at $z = 0$ and $z = 1$ [31], respectively. All the temperatures, and density $\rho(z)$ are normalized with the hot-wall temperature T_h and ρ_r , respectively. This solution is affected by the rarefaction effects present in the slip-flow regime, where the velocity and temperature of the gas adjacent to the walls do not correspond with their wall values. The variation of the temperature jump T_{jump} , defined as the absolute difference between the fluid temperature adjacent to the wall and the temperature of the wall (in the dimensionless format with respect to T_h), at the hot wall, $T_{h,\text{jump}} = 1 - T_0$, and the cold wall, $T_{c,\text{jump}} = T_1 - r$, is shown in Fig. 2(a). The larger growth of the temperature jump T_{jump} at the cold wall indicates the presence of a higher temperature gradient close to the cold wall and is due to conservation of conduction heat flux along the height.

Figure 2(b) shows the profiles of flow properties at a constant rarefaction degree ($Kn = 0.02$), and from $Fr = \frac{v_{\text{th}}^2}{gH} = 1$, strongly stratified, to $Fr = 9$, close to the onset of instability in the full domain. Unlike the temperature profile that remains constant with Fr variations, the density profile changes considerably and brings different states of convection according to the corresponding Fr value. At $Fr = 1$, corresponding to large gravitational forces, the density distribution of the gas is negatively monotonic and dense gas layers are always below less dense layers, and thereby the occurrence of instability is not possible. At $Fr = 2$, a balance between thermal expansion forces and gravitational forces makes the density distribution to be nonmonotonic, where a positive slope emerges in a region close to the cold wall, and at small enough Kn numbers instability may arise in a confined region near the top plate. At a high Froude number, in Fig. 2(b) $Fr = 9$, the density distribution becomes positively monotonic where the denser gas is always above less dense gas layers. This is a necessary condition for onset of instability, and at critical (Fr, Kn) parametric conditions, it can be estimated and quantified based on a constant Rayleigh number.

In RB convection under the Oberbeck-Boussinesq regime, the transition from the conductive to convective regime occurs when the Rayleigh number ($Ra = \frac{\alpha g \Delta T H^3}{\nu k}$) exceeds a critical value Ra_c . In the no-slip regime, the critical value of $Ra_c = 1708$ is obtained by a linear stability analysis of the Oberbeck-Boussinesq equations [19]. For a hard-sphere gas the volume expansion coefficient $\alpha = 1/T$, the kinematic viscosity ν and thermal diffusion coefficient k are obtained at first-order approximation based on the Chapman-Enskog theory for low Knudsen numbers [57]

$$\nu = \frac{5}{16\rho_0 d^2} \sqrt{\frac{k_B m T}{\pi}}, \quad k = \frac{3}{2} \nu, \quad (4)$$

where m is the molecular mass, $\rho_0 = mn = \frac{m}{\sqrt{2\pi} d^2 Kn H}$ is the bulk density used to set the Kn number, and k_B is the Boltzmann constant. Golshtein and Elperin [34] suggested an effective, or average, Rayleigh number based on the assumption that the temperature profile at the conduction state is linear along the vertical direction, and correspondingly the average temperature is $T_{\text{avg}} = \frac{1}{2}(T_h + T_c)$. Within this condition and using the coefficients mentioned for the hard-sphere gas, the Rayleigh number takes the following form:

$$Ra = \frac{2048}{75\pi} \frac{(1-r)}{(1+r)^2 Fr Kn^2}. \quad (5)$$

We have modified this definition by considering the pure conduction solution given as the temperature and density profiles in Eqs. (1) and (2). According to these equations, temperature and density profiles are nonlinear functions, based on the Kn and Fr parameters, along the cell height. Hence, if the average temperature is calculated as $T_{\text{avg}} = \frac{\int T(z)\rho(z)dz}{\int \rho(z)dz}$ using Eqs. (1) and (2), the modified Rayleigh number (Ra_m) now becomes

$$Ra_m = \frac{512}{75\pi} \frac{\Delta T}{T_{\text{avg}}} \frac{1}{Kn^2 Fr_{\text{avg}}}, \quad (6)$$

where $Fr_{\text{avg}} = \frac{2RT_{\text{avg}}}{gH}$. Figure 3 shows the variation of Ra_m/Ra at each constant Ra , according to Eq. (5) and fixed by a set

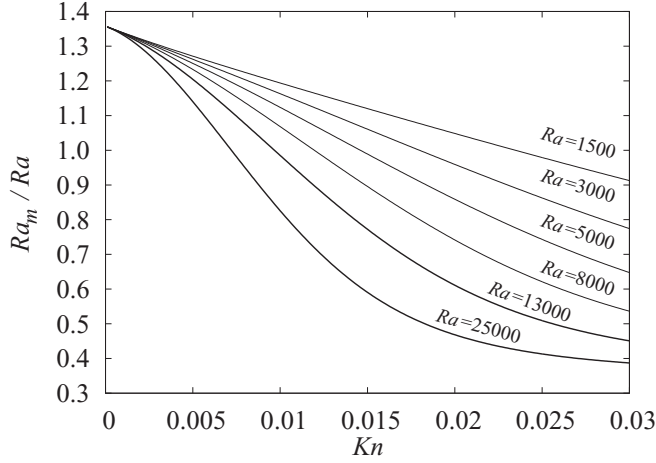


FIG. 3. Ratio of Ra_m to Ra versus Knudsen for the range of $Kn \in [0 - 0.03]$ over which the approximate RB convection zone at temperature ratio $r = 0.1$ is defined. Different lines are for different values of the gravity acceleration, which affects Ra . Each line represents the variation over rarefaction, quantified by Kn , while gravity acceleration g is constant. Note that the modified Rayleigh number Ra_m has a lower value than Ra as rarefaction or gravity increases.

of (g, Kn) parameters, and different Knudsen numbers. Here the Ra parameter changes between 1500 and 25000 as g increases. It is evident that increasing rarefaction decreases the ratio of Ra_m/Ra , and Ra_m/Ra decreases as g increases. Therefore, we expect to generally see lower Ra_m values compared to the traditional definition of Ra in Eq. (5) for cases with higher rarefaction and gravity acceleration.

Transition into the convection regime at high Froude numbers occurs at a constant Rayleigh number, and according to Ref. [50] it occurs at $Ra \approx 1773$, while at low Froude numbers the appearance of a highly stratified flow will suppress convection. The latter limit corresponds to a condition in which the density $\rho(z)$ shows a minimum at the cold wall [31], i.e., $[\frac{d\rho(z)}{dz}]_{z=1} = 0$. Starting from a small Froude number we see that the minimum does not occur within the domain ($0 \leq z \leq 1$) but would only mathematically occur beyond the hot wall, i.e., $\frac{d\rho(z)}{dz} = 0$ for $z > 1$. See Fig. 2(b) with $Fr = 1$ as a highly stratified case at $Kn = 0.02$. Then, while increasing Fr , the position z at which the minimum of density is formed, moves toward to $z = 1$. The flow becomes unstably stratified when $\frac{d\rho(z)}{dz} = 0$ for $z < 1$. See, for example, Fig. 2(b), $Fr = 2$ where the minimum density is found close to the cold wall. As the instability sets in for Fr such that $[\frac{d\rho(z)}{dz}]_{z=1} = 0$, we immediately find

$$-\left(\frac{\xi}{\xi}\right) + \left(\frac{2}{3\eta}\right)^3 \xi^2 = 1, \quad (7)$$

which yields the critical Froude number as

$$Fr_{cr} = \frac{3T_1^{1/2}}{T_0^{3/2} - T_1^{3/2}} \quad (8)$$

with T_0 and T_1 as a function of Kn . The parametric region constrained by low- and high-Froude asymptotes where

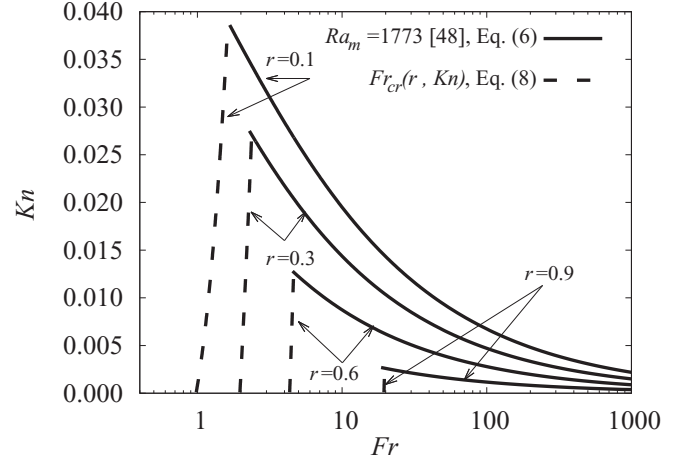


FIG. 4. Demonstration of the zone of convection on the (Fr, Kn) plane at each temperature ratio $r = \frac{T_c}{T_h} = (0.1, 0.3, 0.6, 0.9)$ and outlined via boundaries defined at low and high Froude numbers. These boundaries follow the Ra_m definition in Eq. (6) at high Froude numbers and at low Froude numbers they follow the critical Froude condition defined in Eq. (8). The intersection points of these boundaries, denoted by (Fr_i, Kn_i) , are located at $(1.64, 0.039)$, $(2.38, 0.027)$, $(4.59, 0.013)$, and $(19.51, 0.0026)$ for $r = 0.1, 0.3, 0.6$, and 0.9 , respectively. No convection occurs for $Kn > Kn_i$ for the respective r values as stable stratification of the rarefied gas suppresses the onset of convection. Note the presence of a relatively small area with convection at $r = 0.9$, which is the typical temperature ratio existing in the conventional RB cases in the continuum regime for which the Oberbeck-Boussinesq approximation is valid ($\alpha\Delta T \lesssim 0.2$) [25]. Convection at higher Knudsen values occurs only for low-temperature ratios. For instance at $r = 0.1$, the convection zone includes $Kn \in [0 - 0.03]$, limited by the rarefaction limit of $Kn = 0.03$.

convection is expected to occur, and introduced in Eqs. (6) and (7), is shown in Fig. 4 for several values of r .

Convection zones shown in Fig. 4 determines the importance of choosing the low-temperature ratio $r = 0.1$ in this research. Performing DSMC simulations at low Kn numbers requires high computational resources. Note that the area of the convection zone only extends to a relatively high Kn value, for example $Kn \approx 0.03$ representing the part of the parameter regime where DSMC simulations costs are reasonable, when the smaller temperature ratios are considered. Hence, the temperature ratio $r = 0.1$ would provide feasible DSMC simulations to study convection behavior of a rarefied gas. As a result, the flow regime of interest in this investigation with $r = 0.1$, $Kn \in [0.015 - 0.03]$, is rarefied (with velocity-slip and temperature-jump effects), has large density variations due to the stratification, and is characterized by large non-Oberbeck-Boussinesq effects, i.e., $\alpha\Delta T = \frac{2(1-r)}{(1+r)} \approx 1.64$.

B. Evaluation of the heat transfer

The aim of this section is to define evaluation methods for the calculation of the total heat transfer from bottom to top plate. First, the heat transfer in the bulk, which is composed of the conductive and convective parts, is considered. The underlying assumption is that convective and diffusive transports

are the significant heat transfer processes. Thereby, the energy equation can be expressed as

$$\begin{aligned} \rho c_p \frac{\partial T}{\partial t} + \rho c_p u_x \frac{\partial T}{\partial x} + \rho c_p u_z \frac{\partial T}{\partial z} \\ = \frac{\partial}{\partial x} \left(k_C \frac{\partial T}{\partial x} \right) + \frac{\partial}{\partial z} \left(k_C \frac{\partial T}{\partial z} \right), \end{aligned} \quad (9)$$

where $k_C = k \rho c_p$ is the gas thermal conductivity. Averaging over horizontal sections of the domain, according to $\langle f(x, z) \rangle = \frac{1}{L} \int_0^L f(x, z) dx$, applying the periodic boundary conditions along the horizontal direction, and using of the continuity equation, Eq. (9) becomes

$$\frac{\partial \langle c_p \rho T \rangle}{\partial t} + \frac{\partial \langle c_p \rho u_z T \rangle}{\partial z} = \frac{\partial}{\partial z} \left\langle k_C \frac{\partial T}{\partial z} \right\rangle. \quad (10)$$

According to this description, in the statistically steady state, i.e., when $\frac{\partial \langle c_p \rho T \rangle}{\partial t} = 0$, the conserved heat flux J_z at each position along the cell height z is defined as

$$J_z = \langle \rho c_p u_z T \rangle - \left\langle k_C \frac{\partial T}{\partial z} \right\rangle. \quad (11)$$

The Nusselt number at the cell height z is then defined by making J_z dimensionless using the conductive heat Q_C , i.e., $\text{Nu}_z = \frac{J_z}{Q_C}$. According to the solution obtained for a compressible heat-conducting viscous gas at the pure conduction state, see Eq. (1), Q_C is defined as

$$Q_C = -k_C(z) \frac{\partial T(z)}{\partial z} = -k_C(z) \frac{2\xi}{3(\xi z + \zeta)^{1/3}}. \quad (12)$$

Note that Q_C depends only on (r, Kn) parameters but not on Fr . Finally, in order to have a better statistical average, the Nusselt number in the bulk, Nu_f , is calculated as

$$\text{Nu}_f = \frac{1}{HQ_C} \int_0^H \left(\langle \rho c_p u_z T \rangle - \left\langle k_C \frac{\partial T}{\partial z} \right\rangle \right) dz. \quad (13)$$

Apart from the macroscopic definition of heat transport which is given by Nu_f , we consider also a definition based on the microscopic molecular transport processes at the walls. This evaluation is important as for other thermal flows, nonequilibrium effects on heat transport, such as the anti-Fourier heat transport [59], have been reported. These effects are not taken into account in the bulk evaluation of heat transfer in Eq. (13). Using the simulation methodology of DSMC, it is possible to evaluate the heat flux at the microscopic scale with the physical direct molecular description for which the nonequilibrium effects are implicitly considered. The heat flux at the wall, denoted by q , is defined as the energy exchange between the colliding particles and the wall per unit time and area. The energy exchange in case of a hard-sphere monatomic gas is only based on the translational energy, hence

$$q = \frac{1}{At_s} \left| \sum_{t_s} \frac{1}{2} m (\mathbf{V}_i^2 - \mathbf{V}_r^2) \right|. \quad (14)$$

Here $(\mathbf{V}_i, \mathbf{V}_r)$ are the velocities of a particle before and after interaction with the wall with surface area A , respectively, and t_s is an arbitrary time span in which the kinetic information of the particles hitting the wall are being collected. For the DSMC simulations of the current study, t_s is considered to

be around 60τ , where $\tau = \lambda/V_{\text{th}}$ is the mean-free-flight time. Using Q_C and thermal fluxes evaluated at the cold and hot walls, which we denote by q_c and q_h , respectively, the Nusselt numbers at the cold and hot walls are defined accordingly as

$$\text{Nu}_{w,i} = \frac{q_i}{Q_C} \quad (15)$$

with $i = c$ or $i = h$, representing cold wall and hot wall, respectively.

In this investigation we report the measured Nu values based on the mean and the standard deviation error of the temporal variations, after the steady state is reached. For a set of samples $\{X_1, X_2, X_3, \dots, X_n\}$ the mean \bar{X} and the standard deviation σ_x are calculated based on classical conventions [60] as

$$\bar{X} = \frac{1}{n} \sum_{i=1}^n X_i, \quad \sigma_x^2 = \frac{1}{n-1} \sum_{i=1}^n (X_i - \bar{X})^2. \quad (16)$$

III. THE PARALLEL DSMC CODE

The employment of a computationally intensive numerical method as DSMC becomes practically feasible when computations are done taking advantage of code parallelization. As particle movement and collision events in the DSMC method are managed independently and happen locally, the DSMC routines then are highly suitable for parallelization. The DSMC code in this study, is fully parallelized with message passage interface (MPI) on a three-dimensional Cartesian processor grid, and its development and validation is presented in Ref. [56]. In this code, the physical computational domain is decomposed into groups of cells, and these groups are distributed among parallel processors. Each processor then executes the DSMC algorithm for its corresponding physical space (cells) and containing particles. Communication across processors, in order to transfer particles between each of them, happens as particles cross the physical domain of each processor. Finally, in order to increase the computational efficiency, the computations are separated in two routines. The streaming step and particle interactions with domain boundaries, the inter-process communication operations, and the indexing of the particles within each cell, are performed in the first routine. The second routine performs the collision step, which is based on the ‘‘no time counter’’ (NTC) collision scheme [37], and the evaluation of the hydrodynamic quantities.

TABLE I. Computational information of the simulation cases that are selected according to the typical spatial and temporal discretization rules of the DSMC method [37], where cell size $\Delta x < \frac{\lambda}{2}$, the simulation time step $\Delta t < \frac{\Delta x}{5V_{\text{th}}}$, and the total number of DSMC simulator particles N_t results in 25 or more particles in each cell.

K_n	Grid size ($N_x \times N_z$)	Δt s ($\times 10^{-8}$)	$N_t \times 10^6$
0.015–0.018	400 × 200	4	2
0.020–0.030	200 × 100	4	1

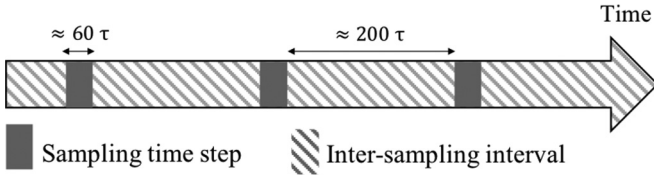


FIG. 5. Time averaging in collecting of particle information used for the evaluation of Nusselt at the walls. The evaluation of $(Nu_{w,c}, Nu_{w,h})$ is based on a sampling time step of about 60τ and the minimum of the intersampling interval is about 200τ . For evaluation of Nusselt values in the bulk (Nu_f) , the instantaneous information is used and the sampling time step corresponds to a single DSMC time step.

IV. RESULTS AND DISCUSSION

In this section, DSMC results obtained for the Rayleigh-Bénard case, as shown in Fig. 1 with a hard-sphere monatomic gas at temperature ratio of $r = 0.1$, aspect ratio of $\Lambda = 2$, and Knudsen number in the range of $0.015-0.030$, are presented. The working fluid is the monatomic argon gas with a molecular mass $m = 6.63 \times 10^{-26}$ kg and a molecular diameter of $d = 3.658 \times 10^{-10}$ m. DSMC calculations start from a uniform initialization at the average temperature ($T = 88K$), and density chosen according to the investigated Kn. Computational informations about DSMC simulations are presented in Table I. In order to obtain Nusselt values at the walls $(Nu_{w,c}, Nu_{w,h})$, sampling, i.e., collecting of particle information during the simulation, is done for a period about 60τ according to the schematic shown in Fig. 5.

A. General overview

A parametric (Fr, Kn) overview of the performed DSMC simulations is shown in Fig. 6. In total around 225 simulations were performed. The simulation times vary according to the (Fr, Kn) parametric conditions. In order to have estimates independent from the size and type of computational resources, simulation times are reported in a comparative format. If the

simulation time for the parameters with $Kn \geq 0.02$ and close to the maximum convection zone, for instance, $Kn = 0.02$ and $Ra_m = 4000$, can be assumed as unity, then parameters with lower rarefaction level, e.g., $0.015 \leq Kn < 0.02$ require a simulation time of 2 to 2.5. In case of parameters close to the zone of onset of convection, i.e., Ra_m close to $Ra_{cr,l} = 1770$, simulations are continued 2 to 4 times longer. Simulations are mostly concentrated near the regions of expected maximum convection, onset of convection (high-Froude limit along the $Ra_m = 1773$ curve, that is mentioned in Ref. [50]), and extinction of convection at the low-Froude limit which is determined by Fr_{cr} defined in Eq. (8).

The effect of rarefaction by varying Kn on RB convection is presented in Figs. 7-9 in terms of the Mach number, velocity, density, temperature fields, and horizontally averaged temperature and density profiles. Additionally, the measured bulk Nusselt number Nu_f over time is displayed in Fig. 10. In Figs. 7-10, the comparisons are made among three simulations with different Knudsen numbers. These particular Knudsen numbers are marked with the blue filled squares in Fig. 6(b), viz. the (Fr, Kn) cases of $(15.53, 0.015)$, $(8.08, 0.02)$, and $(2.87, 0.03)$, at constant $Ra_m \approx 2040$. As rarefaction increases from panels (a)-(c) in Figs. 7, 9, and 10, and from the left to the right column in Fig. 8, the thermal state, while clearly convective for $Kn = 0.015$, transits to the conduction state at $Kn = 0.03$. In order to show a qualitative comparison between the convection intensities of the three cases, the Mach number, defined as $Ma = |V|/\sqrt{\gamma RT}$, of the time-averaged steady-state flow is shown in Fig. 7. Although the two-roll convection structure in Fig. 7 is considered as incompressible (as $Ma \lesssim 0.2$ the flow can be considered as incompressible [61]), for the cases close to the maximum convection state, see Fig. 6(b), the compressibility effect may become relevant. For example, at $Kn = 0.02$ and maximum convection state for $Ra_m \approx 6600$, slight compressibility effects emerge as $Ma_{max} \approx 0.3$.

Contours of instantaneous values of density, temperature, and the horizontal and vertical fluid velocity components

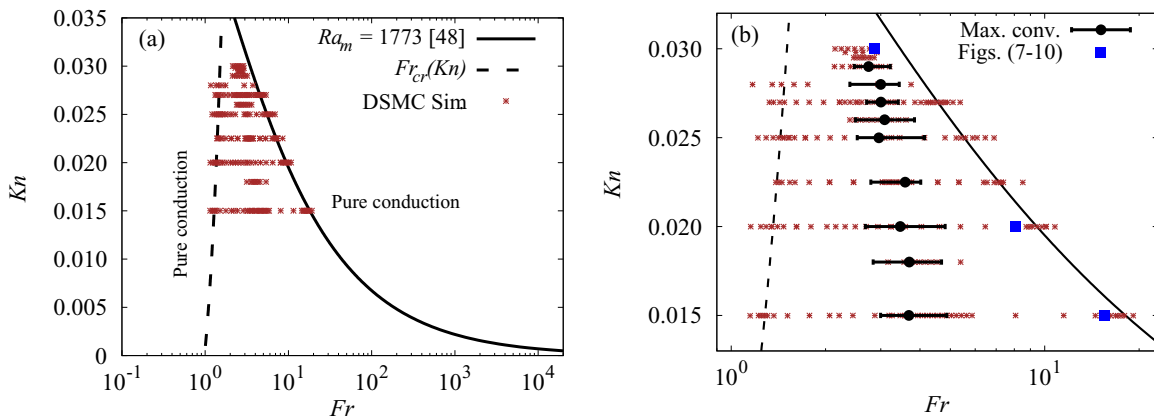


FIG. 6. Overview of the DSMC simulations: (a) a general overview and (b) a zoom on the region of interest. The computational information of these DSMC simulations are summarized in Table I. The distribution of simulations is set in a way to determine the characteristics of the zone of convection, where the interest is on three regions: (i) onset of convection, close to the boundary of $Ra_m = 1773$ and plotted by the black solid line; (ii) maximum of convection, indicated by black circle points with an error margin over Fr; and (iii) cessation of convection, determined by Fr_{cr} defined in Eq. (8) and plotted by the black dashed line.

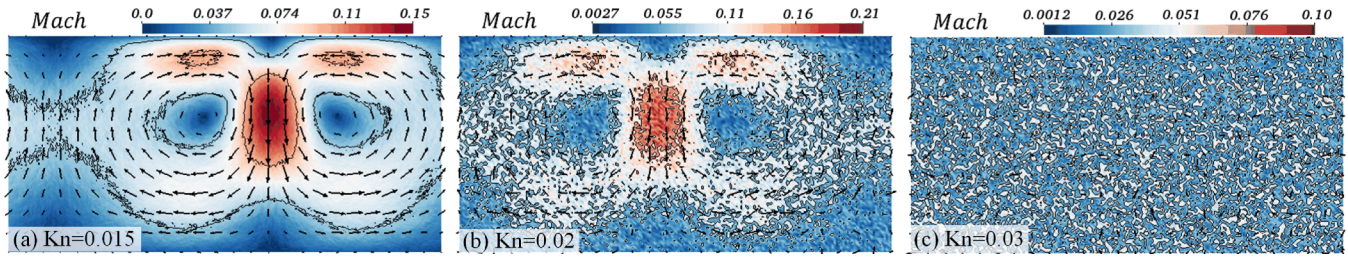


FIG. 7. Mach contour plots overlaid on velocity vectors at a constant $Ra_m \approx 2040$ for (Fr, Kn) cases of $(15.53, 0.015)$, $(8.08, 0.02)$, and $(2.87, 0.03)$. These parametric sets are marked with the blue filled squares in Fig. 6(b). Results are time averaged for 30 time instances once the steady-state solution, based on the temporal Nusselt Nu_f behavior, is reached.

are shown in Fig. 8. It is clear that as rarefaction increases, the macroscopic properties ρ and T show strong signatures of the formation of a conductive state with increasing Kn . In particular, these properties become more homogeneously

distributed in horizontal layers when Kn increases, see the right column.

Transition into the conduction regime due to rarefaction can also be shown based on the one-dimensional temperature

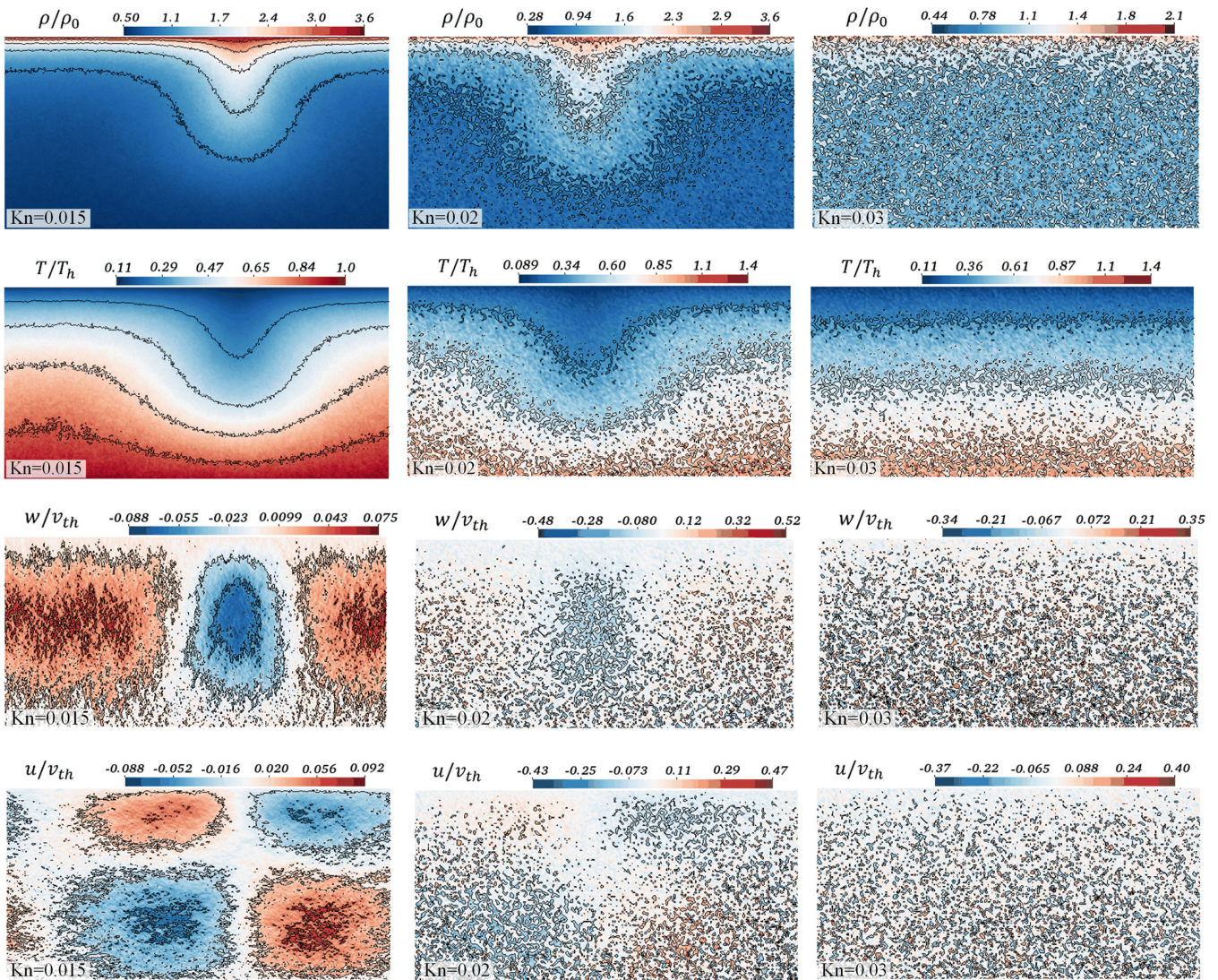


FIG. 8. Contour plots of normalized instantaneous density, temperature, and horizontal and vertical velocity components (u, w) at $Ra_m \approx 2040$ and $Kn = (0.015, 0.02, 0.03)$ for left, center, and right columns, respectively. By increasing rarefaction, the gas properties ρ and T show horizontally homogeneous distributions, a signature of a conductive state.

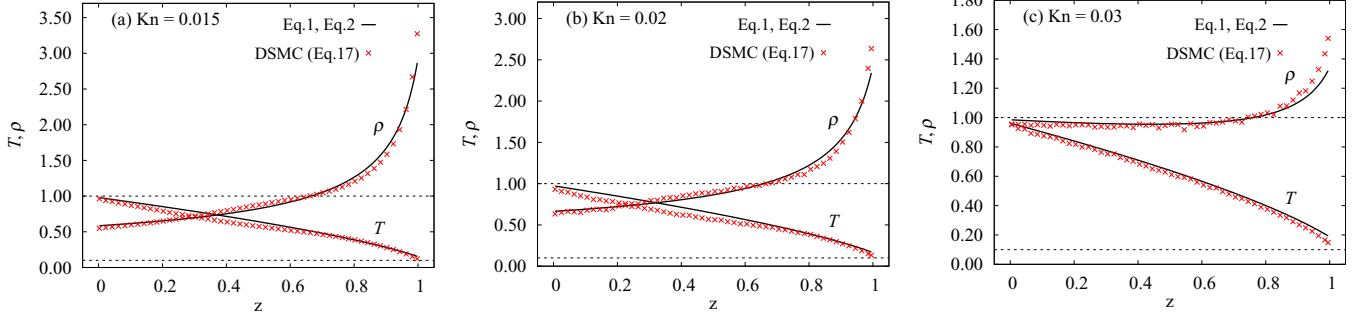


FIG. 9. Dimensionless horizontally averaged temperature and density profiles at $Ra_m \approx 2040$ for $Kn = (0.015, 0.02, 0.03)$. The (Fr, Kn) locations are marked with the blue filled squares in Fig. 6(b). Only a few points of the DSMC results are shown for better visibility. The dashed horizontal lines highlight the temperature values of the walls, $T = (0.1, 1)$. Note that the temperature values of the confined fluid adjacent to the walls do not coincide exactly with the dashed lines. This is recognized as the temperature jump due to rarefaction effects (slip-flow regime).

and density profiles. Figure 9 shows the comparison between these one-dimensional horizontally averaged density and temperature distributions defined as,

$$\langle \rho \rangle = \frac{1}{\rho_0 L} \int_0^L \rho(x, z) dx,$$

$$\langle T \rangle = \frac{1}{T_h L} \int_0^L T(x, z) dx, \quad (17)$$

indicated by the cross symbols in Fig. 9, against the pure conduction solution (solid lines) based on Eqs. (1) and (2). The presence of convection makes the temperature and density profiles slightly deviating from the conductive state. Note also that due to the slip-flow regime, with increasing rarefaction the level of temperature jump also increases. See, for example, the small difference between the horizontal dashed lines representing the wall temperature values $T = (0.1, 1)$ and the red crosses at wall locations, $z = (0, 1)$.

The overall effect of the transition from convective to conductive state can be quantified with the Nusselt number. Figure 10 presents the steady-state variation of Nu_f , defined according to Eq. (13), over time for the three cases $Kn = (0.015, 0.02, 0.03)$ at $Ra_m \approx 2040$. The instantaneous and time-averaged Nusselt numbers, $Nu(t)$ and $\langle Nu \rangle_t = \frac{1}{n} \sum_{i=1}^n Nu(t_i)$, denote the convection state at $Kn =$

$(0.015, 0.02)$ with $\langle Nu \rangle_t$ significantly larger than unity and the conduction state with $\langle Nu \rangle_t \approx 1$, indicating that heat transfer is almost completely governed by conduction, at $Kn = 0.03$. In that case the instantaneous values of $Nu(t)$ varies in the range between 0.96 and 1.06. The strength of convection is measured by the Nusselt numbers defined in Eqs. (13), and (15), where heat transfer is obtained from two different perspectives. These are from the macroscopic bulk flow, Nu_f , and from the molecular processes at the walls, $Nu_{w,c}$ and $Nu_{w,h}$. As stated in Sec. II B, Nu_f is based on the combined conductive and convective heat transport and does not take into account any other nonequilibrium effects. The comparison of the macroscopic and microscopic evaluation methods for Nu_f and the pair $Nu_{w,c}$ and $Nu_{w,h}$, respectively, is provided in Fig. 11. For $Kn = 0.025$ $Nu_{w,c}$ and $Nu_{w,h}$ are compared, showing the exact agreement between the Nusselt evaluations at the two walls. For the $Kn = 0.02$ case, instead a comparison is shown only between the Nusselt evaluation in the bulk (Nu_f) and a Nusselt evaluation at the hot wall ($Nu_{w,h}$) to show the consistency between the two evaluations. It is observed that the different methods provide consistent results. Thereby, it can be concluded that for the cases under consideration the contribution of other thermal effects like heat dissipation and nonequilibrium effects, such as anti-Fourier heat flows, on the heat transfer has a negligible role and convection and diffusion represent the significant heat transfer processes.

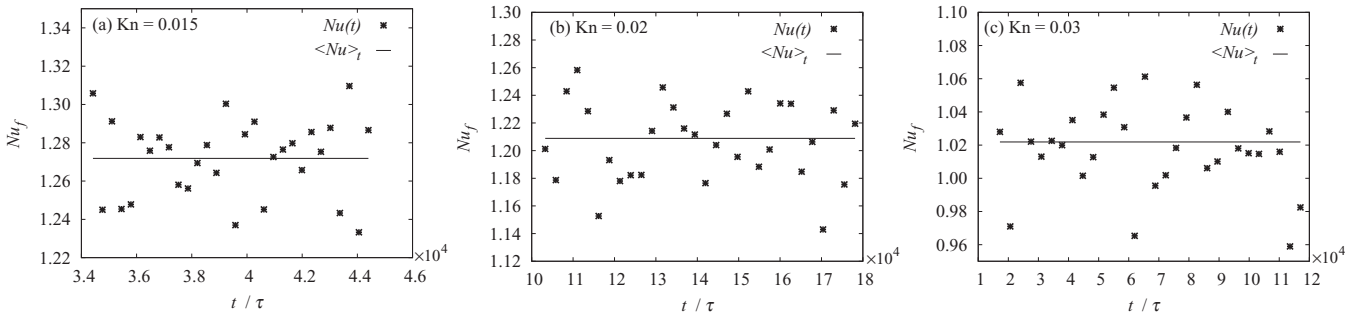


FIG. 10. Variation of Nu_f over time after reaching the steady-state value for $Kn = (0.015, 0.02, 0.03)$ at a constant $Ra_m \approx 2040$. The (Fr, Kn) locations are marked with the blue filled squares in Fig. 6(b). $Nu(t)$ and $\langle Nu \rangle_t$ represent instantaneous and averaged values accordingly. $\langle Nu \rangle_t = (1.27, 1.20, 1.02)$ and standard deviations $\sigma_{Nu} = (0.020, 0.029, 0.027)$, calculated based on Eq. (16) but for time series $\{t_1, \dots, t_n\}$, for the aforementioned sequence of Kn .

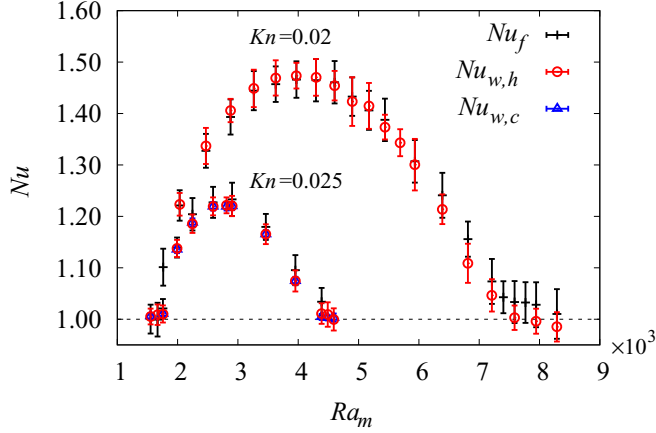


FIG. 11. Comparison of Nusselt values obtained from different methods. The error margin is calculated according to the standard deviation error σ defined in Eq. (16). (i) Nu_f using macroscopic flow-field properties, Eq. (13) and (ii) $Nu_{w,c}$ and $Nu_{w,h}$ using the DSMC methodology in calculating heat exchange at the walls, Eq. (15). Note that the smaller standard deviation error of the Nusselt values from the cold wall is due to the smaller magnitude of temperature when compared to the hot wall. Hence, despite of having different standard deviation errors, it is safe to say that both approaches of Nusselt evaluation can be assumed equivalent under the present conditions.

The general picture of the heat transfer behavior measured by DSMC simulations of the Rayleigh-Bénard instability in rarefied gases is shown in Fig. 12. This behavior is shown in the form of variation of Nu_f at different rarefactions ($0.015 \leq Kn \leq 0.03$) and over the Ra_m range for which the convection zone is defined. A (Nu, Ra) relation according to $Nu = 1 + 1.44(1 - \frac{1708}{Ra_m})$ [62], and valid at $1708 < Ra_m < 5830$, is reported from experimental studies of air in continuum compressible conditions and is added for comparison. At a limited range of low Rayleigh numbers, $Ra_m < 2000$, convection enhancement follows approximately the same trend as these experimental data. This trend is not followed at higher Ra_m values as stratification effects first causes a maximum in convection, see the black dots in Fig. 12, and then a monotonic

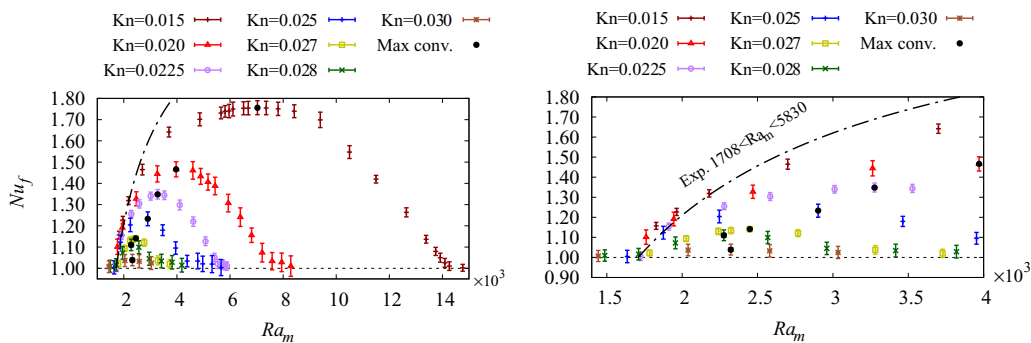


FIG. 12. Nusselt values obtained from macroscopic flow-field properties versus modified Ra_m , see Eq. (6), at $r = 0.1$. The left plot shows the general behavior of Nu_f and the right plot is a zoom on the region of interest at low Ra_m values. Note that the error margin is calculated according to the standard deviation error σ defined in Eq. (16). For the purpose of comparison, experimental $Nu(Ra)$ relation from Ref. [62] for a compressible gas in non-Oberbeck-Boussinesq conditions, which is considered valid in the range of $1708 < Ra_m < 5830$, is also sketched.

TABLE II. Assessment of the critical modified Rayleigh number for the onset of convection, $Ra_{cr,I}$, in the rarefaction range of $0.015 \leq Kn < 0.03$. The error margin is calculated according to the standard deviation error $\sigma_{Ra_{cr,I}}$ defined in Eq. (16).

						$\overline{Ra_{cr,I}}$	$\sigma_{Ra_{cr,I}}$
Kn	0.015	0.02	0.0225	0.025	0.027	—	—
$Ra_{cr,I}$	1785	1770	1750	1760	1785	1770	15

reduction of Nusselt values toward the cessation of convection ($Nu = 1$).

The Rayleigh-Bénard convection zone in this investigation is studied with focus on three stages, (i) onset of convection, (ii) maximum convection, and (iii) cessation of convection, and are discussed in the following sections.

B. Onset of convection

The purpose of this section is to measure the critical modified Rayleigh number, based on the definition given in Eq. (6), for the onset of convection, which is denoted here by $Ra_{cr,I}$, at the high-Fr limit. At each rarefaction degree, thus constant Kn value, the conduction state is made unstable by increasing the value of g which is equivalent to decreasing Fr. We follow here the opposite trajectory, starting from the convective regime and increasing the Froude number. As Fr increases and consequently Ra_m decreases and approaches $Ra_{cr,I}$, the time t_{tr} at which transition from the conduction into the convection state occurs, and which is quantified by Nu, is further delayed, see Fig. 13. This transition is also observed evaluating the total kinetic energy E of the system defined as $E = \frac{1}{2} \sum_{n=1}^{N_{cell}} (\rho_n V_n \mathbf{u}_n^2)$, where \mathbf{u}_n is the macroscopic velocity vector of the cell n , V_n is the cell volume and N_{cell} is the total number of computational cells. According to Figs. 13(c) and 13(d) the energy E of the RB system follows the same trend as the measured heat transfer, see Figs. 13(a) and 13(b). Hence, in the current study, only heat transfer measurements are used to refer to the characteristic behaviors of the system, such as onset or suppression of convection.

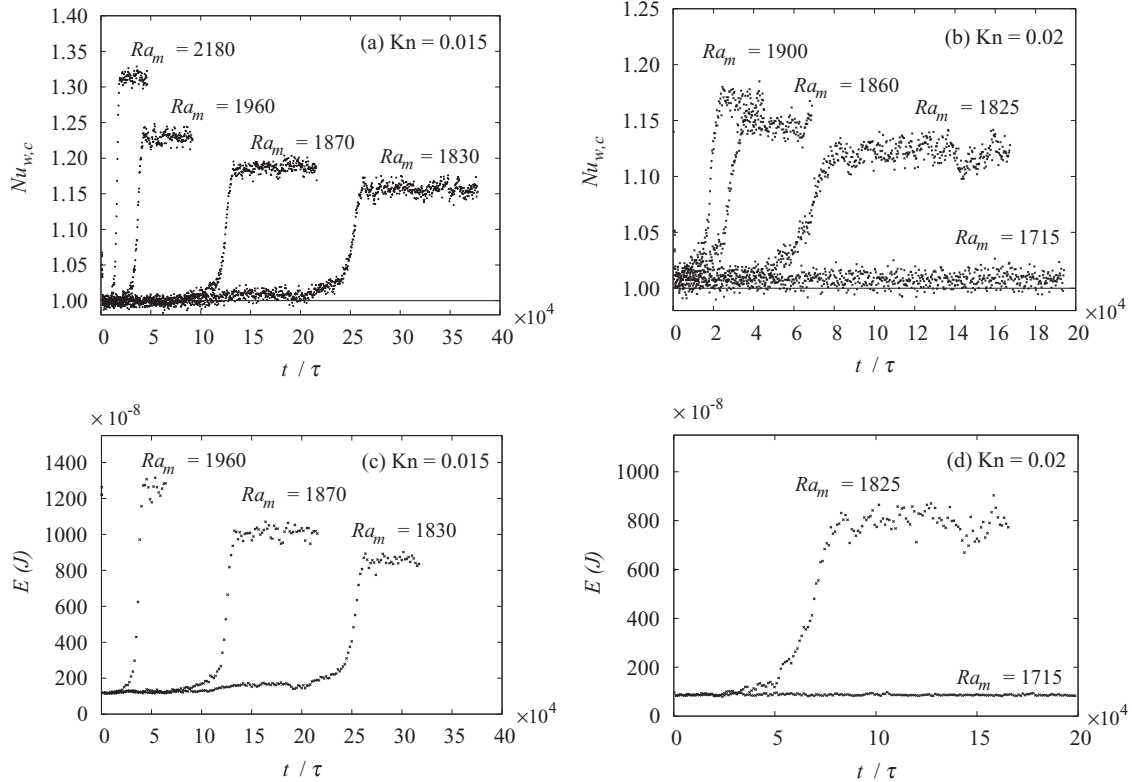


FIG. 13. Temporal behavior of the cold wall Nusselt number $Nu_{w,c}$ and the total kinetic energy E for a set of parameter combinations that are close to the instability limit at high Fr numbers. Note that the cold wall Nusselt number is opted for demonstration as it has lower fluctuations than the hot wall Nusselt number. It is observed that the transition time t_{tr} , normalized with the mean free flight τ , is larger for parameter regimes that are more continuum, thus lower Kn, and closer to the instability limit, e.g., $Ra_{cr,l} \approx 1770$.

Figure 14 presents the long-term steady-state Nusselt values measured at the hot and cold walls for the rarefied RB cases chosen within the range of $Kn \in [0.015 - 0.027]$. At each rarefaction degree we incrementally increase Ra_m and measure the Nusselt value. When the Nusselt value deviates from unity the critical modified Rayleigh for the onset to convection, $Ra_{cr,l}$, is determined, see Table II. According to Table II, for the considered Kn range, the critical modified Rayleigh numbers deviate with a small standard deviation error from the average value $\overline{Ra}_{cr,l}$. Therefore, according to

this evaluation, the critical modified Rayleigh number for the onset of convection in the rarefied range of $0.015 \leq Kn < 0.03$ is determined as $Ra_{cr,l} = 1770 \pm 15$.

C. Maximum convection

We now focus on the maximum convection of a rarefied RB system while varying rarefaction conditions. To this aim, measurements are performed to obtain the maximum convection intensities in terms of Nusselt values at each studied

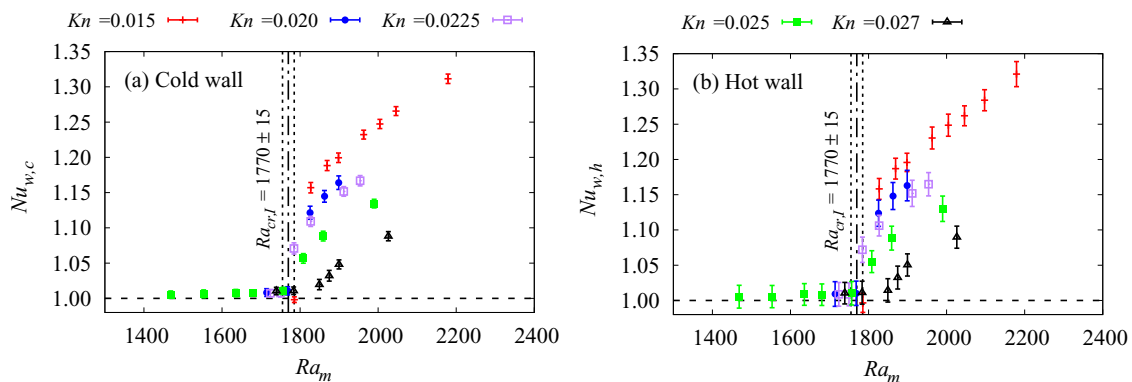


FIG. 14. Transition to convection in proximity of the high-Fr limit, identified via the Nusselt values at the cold and hot walls. The error margin is calculated according to the standard deviation error σ defined in Eq. (16). According to this data set, the onset of convection for parameters in the range of $0.015 \leq Kn < 0.03$ could be extracted and is given in Table II.

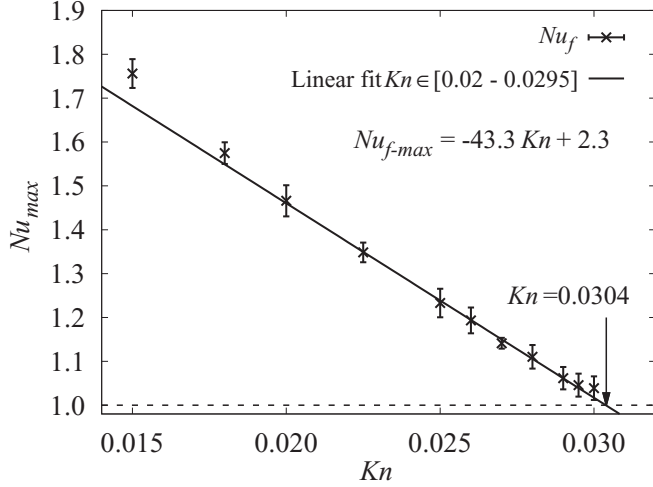


FIG. 15. Maximum Nusselt, Nu_{\max} , obtained at each rarefaction degree Kn . The error margin is calculated according to the standard deviation error σ defined in Eq. (16). Results indicate that the maximum convection of the rarefied RB system tends to decrease linearly for the range of $Kn \in [0.02 - 0.03]$. The intersection of this linear trend with the conduction limit $Nu_{\max} = 1$ coincides with $Kn \approx 0.03$.

rarefaction degree, indicated by Kn , knowing that for each case the maximum convection occurs at different Ra_m . Figure 15 shows a comparison of the maximum Nusselt values, denoted by Nu_{\max} , obtained at each studied rarefaction degree for the range of $Kn \in [0.015 - 0.03]$. A linear dependency of Nu_{\max} on Kn is found for the range of $Kn \in [0.02 - 0.03]$. However, for the less rarefied range, in particular when $Kn \lesssim 0.02$, the maximum convection in the rarefied RB system tends to deviate from the proposed linear trend. They show somewhat higher values of Nu_{\max} . As expected, the linear

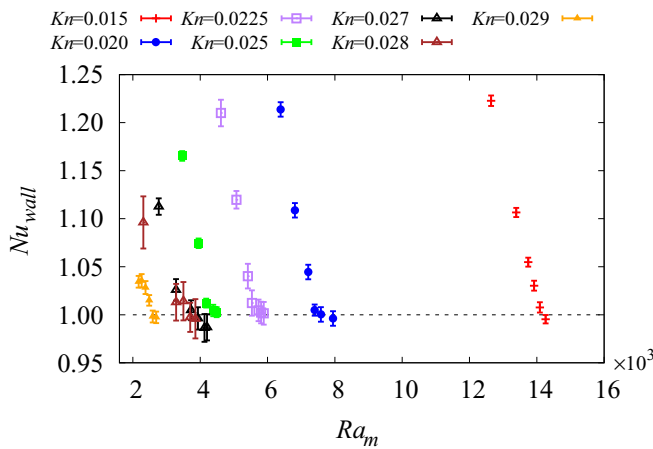


FIG. 16. The heat transfer magnitudes measured for parametric cases at the low-Fr limit and close to the critical Froude number Fr_{cr} , see Eq. (8). The error margin is calculated according to the standard deviation error σ defined in Eq. (16). Based on these points, the critical modified Rayleigh number $Ra_{cr,II}$ for which cessation of convection occurs is assessed for the rarefaction range of $0.015 \leq Kn < 0.03$. The results for $Ra_{cr,II}$ are summarized in Table III.

TABLE III. Assessment of the critical modified Rayleigh number $Ra_{cr,II}$ for the cessation of convection in the rarefaction range of $0.015 \leq Kn < 0.03$. A set of DSMC simulations are performed at each rarefaction degree Kn , while gravity g is being increased incrementally. The critical modified Rayleigh number, for occurrence of the conduction state, i.e., the Nusselt number being close to unity, is then chosen from the simulated cases. In most of the measurements, the determination of $Ra_{cr,II}$ is done with precision about $\Delta Ra_{cr,II} \approx 200$ that is the parametric distance between two consecutive states in which the transition from the convective to the conductive state occurs.

Kn	0.015	0.02	0.0225	0.025	0.027	0.028	0.029
$Ra_{cr,II}$	14091	7400	5671	4343	3511	3285	2541

trend predicts a conduction state with $Nu_{\max} = 1$ due to rarefaction close to the value of $Kn = 0.03$. This estimation agrees closely with the investigation by Stefanov *et al.* [31], in which they reported zero number of convection rolls, which they consider as an indication for the presence of the pure conduction state, generated by the DSMC and the Navier-Stokes finite difference simulations at $Kn = 0.029$ and $Kn = 0.028$, respectively.

D. Limit at low Froude numbers

The suppression of convection at low Fr values is studied looking at the measured heat transfers at the walls. Figure 16 shows the long-term steady-state magnitudes of heat transfer (Nu_{wall}) of the rarefied RB cases. The cessation of convection is presumably due to the emergence of a highly stratified flow, which is analytically bounded by the critical Froude number Fr_{cr} , see Eq. (8). Here, at each rarefaction

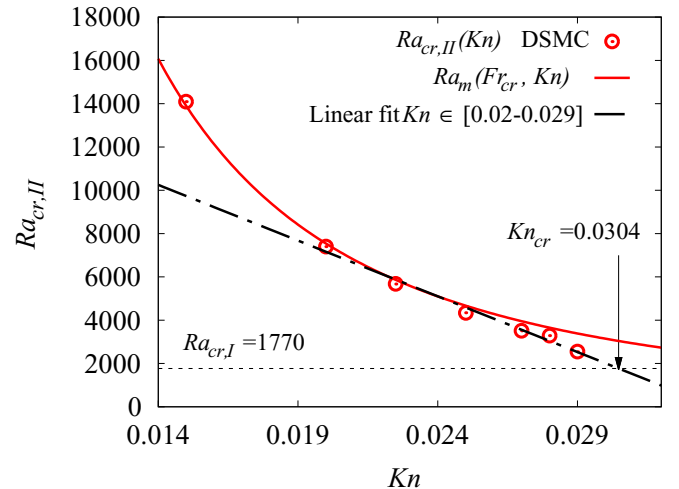


FIG. 17. Critical points in the transition from convective into conductive state for the low-Fr range. Red dots indicate DSMC data for $Ra_{cr,II}$ and the error bars are smaller than the size of the circular symbols. These symbols are compared with the profile of $Ra_m(Fr_{cr}, Kn)$ at the Fr_{cr} condition, see Eq. (8). Note that the linear trend existing at higher rarefactions intersects with the conduction condition of $Ra_m = 1770$ at approximately the hypothetical rarefaction limit of $Kn \approx 0.03$.

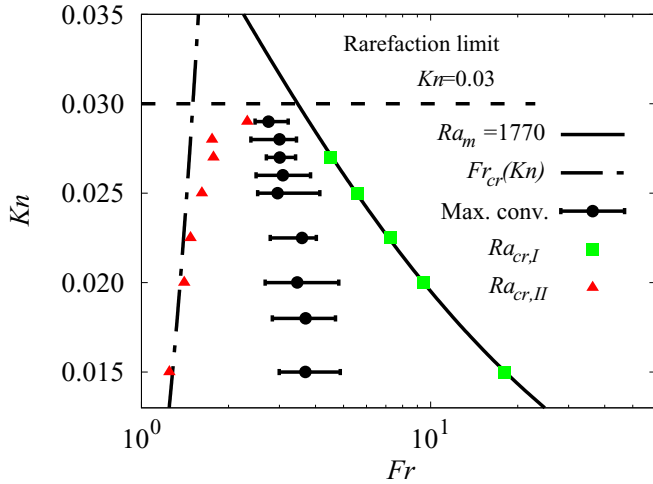


FIG. 18. The convection zone at the rarefied RB problem for $Kn \in [0.015 - 0.03]$ and a fixed temperature ratio of $r = 0.1$. DSMC points obtained in the present work at $Ra_{cr,II}$ are compared with the constant $Ra_m = 1770$, which is the critical value determined via a set of DSMC simulations, see Sec. IV B. Similarly, using the DSMC simulations, the values for $Ra_{cr,II}$ are obtained and compared with the condition posed by Fr_{cr} , see Eq. (8). Note that the zone of convection is also bounded with the rarefaction limit of $Kn \approx 0.03$.

degree Kn , the value of Ra_m is incrementally increased with increasing gravity g , and the flow regime approaches the condition for cessation of convection posed by Fr_{cr} . Thereby, the cases in which the convection state changes into the conduction state are approximately recognized. The $Ra_{cr,II}$ is defined as the critical modified Rayleigh number in which this transition at the low- Fr limit occurs, and is given in Table III.

In order to better distinguish this behavior for the rarefaction range of $Kn \gtrsim 0.02$, $Ra_{cr,II}$ is shown versus the rarefaction degree Kn in Fig. 17. According to this figure, for the higher rarefaction range ($Kn \gtrsim 0.02$) a linear decrease of $Ra_{cr,II}$ versus Kn is recognized, which also seems to deviate from the prediction based on Fr_{cr} . In this figure, with the assumption that at higher rarefactions ($Kn \gtrsim 0.02$), the conduction limits of the high ($Ra_{cr,I} = 1770$) and low ($Ra_{cr,II}$) Froude numbers will asymptotically intersect, the mentioned linear decrease of $Ra_{cr,II}$ is extrapolated. The two limits ($Ra_{cr,I}, Ra_{cr,II}$) then intersect at a point close to the rarefaction limit of $Kn \approx 0.03$, which indicates the conduction limit imposed by the rarefaction condition. See also Fig. 15 where extrapolation of Nusselt values in the maximum convection state asymptotically intersects with the conduction condition at a point close to the rarefaction limit $Kn \approx 0.03$.

Finally, using the data presented in this research, the convection zone in (Fr, Kn) plane can be updated. Figure 18 shows the parametric locations obtained by the DSMC simulations to determine the regions of (i) onset of convection, (ii) maximum convection, and (iii) cessation of convection.

V. CONCLUSION

This investigation addressed the behavior of Rayleigh-Bénard convection of a rarefied gas using DSMC simulations for $r = \frac{T_c}{T_h} = 0.1$. Both macroscopic- and microscopic-based measurements of the heat transfer were done for the bulk fluid and also at the cold and hot walls. These measurements were applied to determine the limits within the parametric space for which the onset and cessation of convection as well as the maximum convection occurs.

It was shown that the maximum convective heat transfer at each rarefaction degree linearly decreases in the $0.02 \leq Kn < 0.03$ range. This linear trend intersects the conduction state at $Kn \approx 0.03$.

By taking into account the non-Boussinesq effects as obtained from the pure conduction solution of the RB compressible “slip-model,” a modified Rayleigh number (Ra_m) definition is proposed that takes into account the nonlinear distribution of temperature at the pure conduction state. It was observed that the Rayleigh range for which the onset of convection occurs is small enough to be represented by a single constant Ra_m value. DSMC simulations for the rarefied range of $Kn \geq 0.015$ showed that the critical modified Rayleigh number for the onset of convection, $Ra_{cr,I}$, can be closely approximated as $Ra_{cr,I} = 1770 \pm 15$.

At low Froude numbers corresponding to strongly stratified states, the critical modified Rayleigh numbers $Ra_{cr,II}$ in which a convective state changes into a conductive state are determined. Non-Oberbeck-Boussinesq effects in this rarefied and highly stratified regime makes no longer possible to reach a single nondimensional parameter describing the cessation of convection. Despite this fact, performing DSMC simulations at each rarefaction degree, a linear dependency between $Ra_{cr,II}$ and Kn has been observed for $Kn \gtrsim 0.02$. How the results for $Ra_{cr,II}$ are affected by stratification and what is due to rarefaction is not fully clear yet. For the low- Kn regime, it might be useful to explore this transition between the convective and conductive state from the continuum system. Is the second transition, at $Ra_{cr,II}$, still present for very small Kn ? Although this is outside the scope of the present work and not feasible with DSMC future investigations are required to shed light on this particular issue. At higher rarefaction conditions, the aforementioned linear trend between $Ra_{cr,II}$ and Kn intersects with the onset of the conduction limit, defined by $Ra_{cr,I} = 1770$, at a parametric zone close to the rarefaction limit of $Kn \approx 0.03$.

[1] J. Marshall and F. Schott, Open-ocean convection: Observations, theory, and models, *Rev. Geophys.* **37**, 1 (1999).
 [2] G. Vallis, *Atmospheric and Oceanic Fluid Dynamics* (Cambridge University Press, Cambridge, UK, 2017).

[3] R. Ferrari and D. Ferreira, What processes drive the ocean heat transport? *Ocean Modell.* **38**, 171 (2011).
 [4] J. Wyngaard, *Turbulence in the Atmosphere* (Cambridge University Press, Cambridge, UK, 2010).

- [5] B. Stevens, Atmospheric moist convection, *Annu. Rev. Earth Planet Sci.* **33**, 605 (2005).
- [6] F. Busse and C. Carrigan, Laboratory simulation of thermal convection in rotating planets and stars, *Science* **191**, 81 (1976).
- [7] F. Busse, Convective flows in rapidly rotating spheres and their dynamo action, *Phys. Fluids* **14**, 1301 (2002).
- [8] Å. Nordlund, R. Stein, and M. Asplund, Solar surface convection, *Living Rev. Sol. Phys.* **6**, 2 (2009).
- [9] K. Julien, A. Rubio, I. Grooms, and E. Knobloch, Statistical and physical balances in low Rossby number Rayleigh–Bénard convection, *Geophys. Astrophys. Fluid Dyn.* **106**, 392 (2012).
- [10] K. Julien, E. Knobloch, A. M. Rubio, and G. M. Vasil, Heat Transport in Low-Rossby-Number Rayleigh–Bénard Convection, *Phys. Rev. Lett.* **109**, 254503 (2012).
- [11] D. Nieves, A. Rubio, and K. Julien, Statistical classification of flow morphology in rapidly rotating Rayleigh–Bénard convection, *Phys. Fluids* **26**, 086602 (2014).
- [12] S. Stellmach, M. Lischper, K. Julien, G. Vasil, J. S. Cheng, A. Ribeiro, E. M. King, and J. M. Aurnou, Approaching the Asymptotic Regime of Rapidly Rotating Convection: Boundary Layers Versus Interior Dynamics, *Phys. Rev. Lett.* **113**, 254501 (2014).
- [13] R. Kunnen, R. Ostilla-Mónico, E. van der Poel, R. Verzicco, and D. Lohse, Transition to geostrophic convection: The role of the boundary conditions, *J. Fluid Mech.* **799**, 413 (2016).
- [14] H. Rajaei, R. Kunnen, and H. Clercx, Exploring the geostrophic regime of rapidly rotating convection with experiments, *Phys. Fluids* **29**, 045105 (2017).
- [15] S. Kakaç, H. Yüncü, and K. Hijikata, *Cooling of Electronic Systems*, Vol. 258 (Springer, Berlin, 2012).
- [16] A. Adham, N. Mohd-Ghazali, and R. Ahmad, Thermal and hydrodynamic analysis of microchannel heat sinks: A review, *Renew. Sust. Energy Rev.* **21**, 614 (2013).
- [17] C. Wagner and N. Harned, Euv lithography: Lithography gets extreme, *Nat. Photon.* **4**, 24 (2010).
- [18] R. Abhari, A. Giovannini, B. Rollinger, and D. Bleiner, Extreme ultraviolet light source with a debris-mitigated and cooled collector optics (2014), US Patent 8,723,147.
- [19] S. Chandrasekhar, *Hydrodynamic and Hydromagnetic Stability* (Clarendon Press, Oxford, 1961).
- [20] P. Drazin, *Introduction to Hydrodynamic Stability*, Vol. 32 (Cambridge University Press, Cambridge, UK, 2002).
- [21] E. Bodenschatz, W. Pesch, and G. Ahlers, Recent developments in Rayleigh–Bénard convection, *Annu. Rev. Fluid Mech.* **32**, 709 (2000).
- [22] S. Grossmann and D. Lohse, Prandtl and Rayleigh number dependence of the Reynolds number in turbulent thermal convection, *Phys. Rev. E* **66**, 016305 (2002).
- [23] G. Ahlers, S. Grossmann, and D. Lohse, Heat transfer and large scale dynamics in turbulent Rayleigh–Bénard convection, *Rev. Mod. Phys.* **81**, 503 (2009).
- [24] D. Lohse and K. Xia, Small-scale properties of turbulent Rayleigh–Bénard convection, *Annu. Rev. Fluid Mech.* **42**, 335 (2010).
- [25] F. Chillà and J. Schumacher, New perspectives in turbulent Rayleigh–Bénard convection, *Eur. Phys. J. E* **35**, 58 (2012).
- [26] A. Oberbeck, Über die wärmeleitung der flüssigkeiten bei berücksichtigung der strömungen infolge von temperaturdifferenzen, *Ann. Phys.* **243**, 271 (1879).
- [27] J. Boussinesq, *Théorie analytique de la chaleur*, Vol. 2 (Gauthier-Villars, Paris, 1903).
- [28] L. Landau and E. Lifshitz, *Fluid Mechanics* (Pergamon Press, Oxford, 1987).
- [29] G. Karniadakis, A. Beskok, and N. Aluru, *Microflows and Nanoflows: Fundamentals and Simulation*, Vol. 29 (Springer, Berlin, 2006).
- [30] Y. Sone, K. Aoki, and H. Sugimoto, The Bénard problem for a rarefied gas: Formation of steady flow patterns and stability of array of rolls, *Phys. Fluids* **9**, 3898 (1997).
- [31] S. Stefanov, V. Roussinov, and C. Cercignani, Rayleigh–Bénard flow of a rarefied gas and its attractors. I. Convection regime, *Phys. Fluids* **14**, 2255 (2002).
- [32] D. Gray and A. Giorgini, The validity of the boussinesq approximation for liquids and gases, *Int. J. Heat Mass Transf.* **19**, 545 (1976).
- [33] S. Horn, O. Shishkina, and C. Wagner, On non-oberbeck-boussinesq effects in three-dimensional rayleigh-bénard convection in glycerol, *J. Fluid Mech.* **724**, 175 (2013).
- [34] E. Golshtein and T. Elperin, Convective instabilities in rarefied gases by direct simulation Monte Carlo method, *J. Thermophys. Heat Transf.* **10**, 250 (1996).
- [35] G. Bird, Approach to translational equilibrium in a rigid sphere gas, *Phys. Fluids* **6**, 1518 (1963).
- [36] G. Bird, *Molecular Gas Dynamics* (Oxford University Press, Oxford, 1976).
- [37] G. Bird, *Molecular Gas Dynamics and the Direct Simulation of Gas Flows*, Vol. 5 (Clarendon Press Oxford, London, 1994).
- [38] G. Bird, Perception of numerical methods in rarefied gasdynamics, *Prog. Astronaut. Aeronaut.* **118**, 211 (1989).
- [39] S. Stefanov, Particle Monte Carlo algorithms with small number of particles in grid cells, in *Numerical Methods and Applications* (Springer, Berlin, 2011), pp. 110–117.
- [40] G. Bird, Visual DSMC program for two-dimensional and axially symmetric flows, *The DS2V Program Users Guide* (GAB Consulting, Sydney, 2006).
- [41] K. Nanbu, Direct simulation scheme derived from the Boltzmann equation. i. Monocomponent gases, *J. Phys. Soc. Jpn.* **49**, 2042 (1980).
- [42] W. Wagner, A convergence proof for Bird’s direct simulation Monte Carlo method for the Boltzmann equation, *J. Stat. Phys.* **66**, 1011 (1992).
- [43] A. Garcia, Hydrodynamic fluctuations and the direct simulation Monte Carlo method, in *Microscopic Simulations of Complex Flows* (Springer, Berlin, 1990), pp. 177–188.
- [44] S. Stefanov and C. Cercignani, Monte Carlo simulation of Bénard instability in a rarefied gas, *Eur. J. Mech. B/Fluids* **11**, 543 (1992).
- [45] C. Cercignani, M. Giurin, and J. Struckmeier, The Rayleigh–Bénard convection in rarefied gases, AGTM Report 192, TU Kaiserslautern (1998).
- [46] S. Stefanov, V. Roussinov, and C. Cercignani, Rayleigh–Bénard flow of a rarefied gas and its attractors. III. Three-dimensional computer simulations, *Phys. Fluids* **19**, 124101 (2007).
- [47] S. Stefanov, V. Roussinov, and C. Cercignani, Rayleigh–Bénard flow of a rarefied gas and its attractors. II. Chaotic and periodic convective regimes, *Phys. Fluids* **14**, 2270 (2002).
- [48] T. Watanabe, H. Kaburaki, and M. Yokokawa, Simulation of a two-dimensional Rayleigh–Bénard system using the direct simulation Monte Carlo method, *Phys. Rev. E* **49**, 4060 (1994).

- [49] J. Zhang and J. Fan, Kinetic study of the Rayleigh-Bénard flows, *Chin. Sci. Bull.* **54**, 364 (2009).
- [50] A. Manela and I. Frankel, On the Rayleigh-Bénard problem in the continuum limit, *Phys. Fluids* **17**, 036101 (2005).
- [51] P. Tzeng and M. Liu, Direct-simulation Monte Carlo modeling on two-dimensional Rayleigh-Bénard instabilities of rarefied gas, *Numer. Heat Transfer, Part A* **47**, 805 (2005).
- [52] A. Manela and I. Frankel, On the rayleigh-bénard problem in the continuum limit: Effects of temperature differences and model interaction, *Phys. Fluids* **17**, 118105 (2005).
- [53] A. Manela and I. Frankel, On the rayleigh-bénard problem: Dominant compressibility effects, *J. Fluid Mech.* **565**, 461 (2006).
- [54] Y. Ben-Ami and A. Manela, Effect of heat-flux boundary conditions on the Rayleigh-Bénard instability in a rarefied gas, *Phys. Rev. Fluids* **4**, 033402 (2019).
- [55] Y. Fang and W. Liou, Unsteady disturbances in micro Rayleigh-Bénard flows using direct simulation Monte Carlo method, *Int. J. Aeroacoust.* **17**, 425 (2018).
- [56] G. Di Staso, Hybrid discretizations of the Boltzmann equation for the dilute gas flow regime, Ph.D. thesis, Eindhoven University of Technology, 2018.
- [57] S. Chapman and T. Cowling, *The Mathematical Theory of Non-uniform Gases* (Cambridge University Press, Cambridge, 1970).
- [58] S. Albertoni, C. Cercignani, and L. Gotusso, Numerical evaluation of the slip coefficient, *Phys. Fluids* **6**, 993 (1963).
- [59] B. John, X. Gu, and D. Emerson, Investigation of heat and mass transfer in a lid-driven cavity under nonequilibrium flow conditions, *Numer. Heat Transfer, Part B* **58**, 287 (2010).
- [60] B. Martin, *Statistics for Physical Sciences: An Introduction* (Academic Press, San Diego, CA, 2012).
- [61] D. Young, B. Munson, T. Okiishi, and W. Huebsch, *A Brief Introduction to Fluid Mechanics* (John Wiley & Sons, New York, 2010).
- [62] Y. Jaluria, *Natural Convection, Heat and Mass Transfer* (Pergamon Press, London, 1980).